Rational Design of Carbon-Based Porous Aerogels with Nitrogen Defects and Dedicated Interfacial Structures toward Highly Efficient CO₂ Greenhouse Gas Capture and Separation

Liang Wang, Shiying Fan, Xinyong Li,* Moses O. Tadé, and Shaomin Liu

Read Online

ACCESS | Metrics & More | Article Recommendations | SI Supporting Information

ABSTRACT: CO₂ capture from flowing flue gases through adsorption technology is essential to reduce the emission of CO₂ to the atmosphere. The rational design of highly efficient carbon-based absorbents with interfacial structures containing interconnected porous structures and abundant adsorption sites might be one of the promising strategies. Here, we report the synthesis of nitrogen-doped carbon aerogels (NCAs) via prepolymerized phenol−melamine−formaldehyde organic aerogels (PMF) by controlling the addition amount of ZnCl₂ and the precursor M/P ratio. It has been revealed that NCAs with a higher specific surface area and interconnected porous structures contain a large amount of pyridinic nitrogen and pyrrolic nitrogen. These would act as the intrinsic adsorption sites for highly effective CO₂ capture and further improve the CO₂/N₂ separation efficiencies. Among the prepared samples, NCA-1-2 with a high micropore surface area and high nitrogen content exhibits a high CO₂ adsorption capacity (4.30 mmol g⁻¹ at 0 °C and 1 bar) and CO₂/N₂ selectivity (36.5 at 25 °C, IAST). Under typical flue gas conditions (25 °C and 1.01 bar), equilibrium gas adsorption analysis and dynamic breakthrough measurement associated with a high adsorption capacity of 2.65 mmol g⁻¹ at 25 °C and 1.01 bar and 0.81 mmol g⁻¹ at 25 °C and 0.15 bar. This rationally designed N-doped carbon aerogel with specific interfacial structures and high CO₂ adsorption capacity, high selectivity, and adsorption performance remained pretty stable after multiple uses.
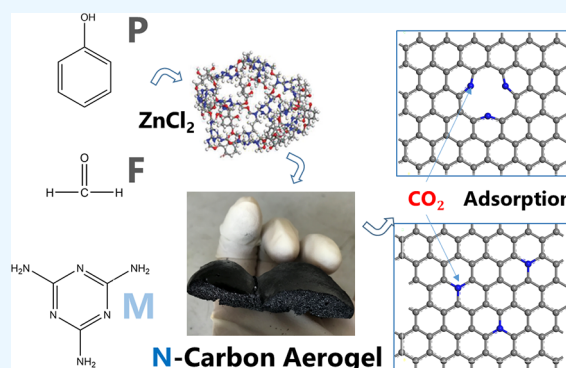
1. INTRODUCTION

It has been well recognized that human emissions of carbon dioxide and other greenhouse gases are a primary driver of climate change, which is one of the world's most critical challenges. Hence, seeking a highly efficient fixing and capturing strategy of CO₂ using adsorption and conversions under mild conditions seems to be the most attractive option.[1−10] Generally, this requires the adsorbent to have marvelous adsorption kinetics, high adsorption capacity, good selectivity, and long-term stability under actual working conditions.[11−14] Currently, rationally designing carbon-based absorbents with interfacial structures, abundant activation sites, and specific adsorptions characteristics has attracted enormous scientific attention.

For the structure-tailing of carbon-based materials, scientists have developed several fabrication strategies to tune the crossing carbon frameworks and porous and interfacial structures with the aim of generating a bunch of activation and adsorptions sites toward efficient capturing of carbon dioxide.[15,16] Specifically, as one member of carbon-based porous materials, the carbon aerogels could be tuned into specific structures for a wide range of applications including adsorption, catalysis, and energy storage and conversions.[17−26]

They have been proven to be one of the most promising carbon-based adsorbents with outstanding performance, including superior adsorption characteristics. It is inferred from previous studies that the specific structural features of carbon aerogels are primarily attributed to their unique interfacial and hierarchical structures as derived from the cracking organic aerogel, which started from a liquid solution and culminated in the formation of a nanostructured material composed of a single piece. The creation and sequential formation of hierarchical pore structures usually depend on the growth and aggregated reaction of cross-linked polymer clusters by the appropriate monomeric precursor.[27,28] Scientists have devoted numerous efforts to modulating the aforementioned hierarchical pore structures via activations and sequential carbonization processes. Antonietti and co-workers reported a hypersaline template method for synthesizing

phenol−formaldehyde resins based on an organic aerogel with an interconnected macroscopic structure and preparing carbon aerogels materials by using the organic aerogel as a precursor.[29] This method avoids the complicated preparation process of traditional carbon aerogels and regulates the porous structure by using $ZnCl_2$ as an activation agent.[29] The resultant carbon aerogels show promising potential in the adsorption/ separation of organic pollutants.

Other potential strategies, such as adulterating heteroatoms into the carbon matrix, also aroused great interest due to their features of increasing the number of adsorption sites, raising gas storage capacity, and eventually improving adsorption/ separation performance. Generally, while the characteristics of CO_2 molecules are considered, the critical interaction between porous carbon-based absorbents and the uptake of CO_2 molecules could be significantly enhanced by rationally constructing CO_2-philic sites.[30,31] The introduction of nitrogen into carbon materials as the active base center has been well proven to increase the weak chemical interaction between weakly acidic CO_2 molecules and the carbon-based material. Hence, the adsorption capacity and selectivity of CO_2 can be accordingly improved remarkably. Extensive literature has been reported regarding the design and synthesis of nitrogen-disturbed carbon-based materials by employing dedicated nitrogen-containing precursors containing biomass, waste papers, nitrogen-containing compounds, etc.[32−35] Most of these precursors only serve as nitrogen resources and may incur various nitrogen defects distributed within the surface and bulk of carbon materials.[36,37] It is inferred from previous studies that to reduce the structural shrinkage and nitrogen loss during pyrolysis and form a hierarchical porous structure with a high nitrogen residue, the key is to design nitrogen-containing polymers with rigid backbones.[38] The high nitrogen content usually can result in the formation of melamine species that possess the advantage of being the most competitive choice for carbon materials. Furthermore, melamine can accordingly generate melamine−formaldehyde resins with formaldehyde sections, and its synthetic methodology is very similar to that of phenol−formaldehyde resins. Interestingly, numerous investigations indicated that a proper combination strategy of cross-linking the phenol−formaldehyde resins and melamine−formaldehyde resins followed by producing 3D cross-linking networks structurally similar to organic polymers provides nearly perfect rigidity for the entire structure of the carbon materials.[39,40] Furthermore, the regulation of pores is also significant for tuning the amazing structures toward carbon dioxide adsorptions, which could be generally realized by controlling activation conditions, e.g., the activator amount, activation time, and working temperatures.[41,42] Therefore, it would be feasible to balance the adsorption capacity and selectivity toward CO_2 capture under working dynamic flow conditions by alternatively adjusting and tailoring the surficial and interfacial structures including nitrogen defects of the porous carbon materials.

Herein, a series of organogels homogeneously mixed with $ZnCl_2$ were prepared by using low-cost phenol, melamine, and formaldehyde as precursors and by controlling the amount of $ZnCl_2$ added and the M/P ratio of the precursor. The homogeneously dispersed $ZnCl_2$ in the organic aerogels can be used as a foaming agent and etching agent directly together with PMF to prepare nitrogen-doped carbon aerogels (NCAs) through the carbonization activation process. The effects of precursor component molecular proportions on the structure,

morphology, physicochemical properties, and features of the nitrogen defects within carbon-based materials were accordingly investigated and summarized in terms of the research outcomes. The as-prepared porous carbon aerogel with high specific surface area, micropore volume (in particular, ultramicropore volume), and interfacial structures containing anionic nitrogen defects showed fascinating CO_2 adsorption capacity in various working conditions, including static adsorptions, dynamic adsorptions, and gas-mixture separations. It is believed that the obtained novel N-disturbed carbon aerogel (NCA) with plentiful surficial−interfacial structures and specific physical−chemical features including hierarchical porosity and rich adsorption site would find dedicated and promising utilization toward the highly efficient capture of CO_2 greenhouse gas species.

2. MATERIALS AND METHODS

2.1. Chemicals. The materials were used as received without further purification. Deionized water was used in all the experiments. All chemicals and solvents were purchased from Shanghai Chemical Reagent Co., Ltd.

2.2. Synthesis of Organic Aerogels. The general synthesis process of organic aerogels (OAs) has been accordingly summarized as follows: Phenolic formaldehyde (PF) resins were obtained by the reaction of P and F. P is reactive at the ortho sites, allowing F to attach to the ring. In the process of synthesis, P and F first generate a monomer with a large number of hydroxymethyl groups through an addition reaction, then dehydrate and condense at a high temperature to form methylene and methyl ether bridges, and finally form a cross-linked polymer network.[37] The melamine−formaldehyde (MF) resin is also a common polymer that has been industrially produced, and its synthesis methodology is very similar to PF. $ZnCl_2$ was added to PF + MF solutions as a Lewis acid catalyst, and a white sticky sol was synthesized (Figure S1a). To study the effect of M addition on the polymerization of organic aerogels and the nitrogen content in carbon aerogels, four different M/P molar ratios (PF/MF = 4:1, 2:1, 1:1, and 1:2) were selected. The molar ratios of F/P and F/M were fixed at 1:1 and 3:1, respectively, in all the cases. Solution A, which contained P and F, was stirred for 2 h at 40 °C. Separately, solution B, which included M and F, was stirred for 10 min at 80 °C. After that, solutions A and B were mixed and stirred at 40 °C for 1 h. Then, 2 mL of the mixed solution (A + B) was obtained and slowly dropped into a glass vial that contained 8 g of $ZnCl_2$. To avoid drastic heat release, $ZnCl_2$ was dissolved in an ice bath. The glass vials that contained the white sticky sol were sealed in a 50 mL Teflon-lined autoclave and heated at 160 °C for 8 h. Then, the black monolith PMF-X (X = 4-1, 2-1, 1-1, 1-2) OAs were prepared (Figure S1b−d).

2.3. Synthesis of NCAs. The obtained PMF-X (X = 4-1, 2-1, 1-1, 1-2) was heated under a flowing nitrogen atmosphere at 900 °C without any drying process (heating rate: 3 °C min⁻¹) for 2 h. Next, the products were purified by HCl (1 M) with a magnetic stirrer for 12 h, followed by multiple rinsing with deionized water, and dried at 110 °C overnight. The as-resulted samples were denoted as NCAs (NCA-X). The synthesis of CA is similar to that of NCA-X, without adding solution B to the polymeric precursor solution. The synthesis strategy of NCA_0-2-1 and NCA_4-2-1 has been kept the same as that of NCA-2-1 (NCA_8-2-1), in which specific amounts of $ZnCl_2$ (0, 4, and 8 g) were accordingly into the reactions
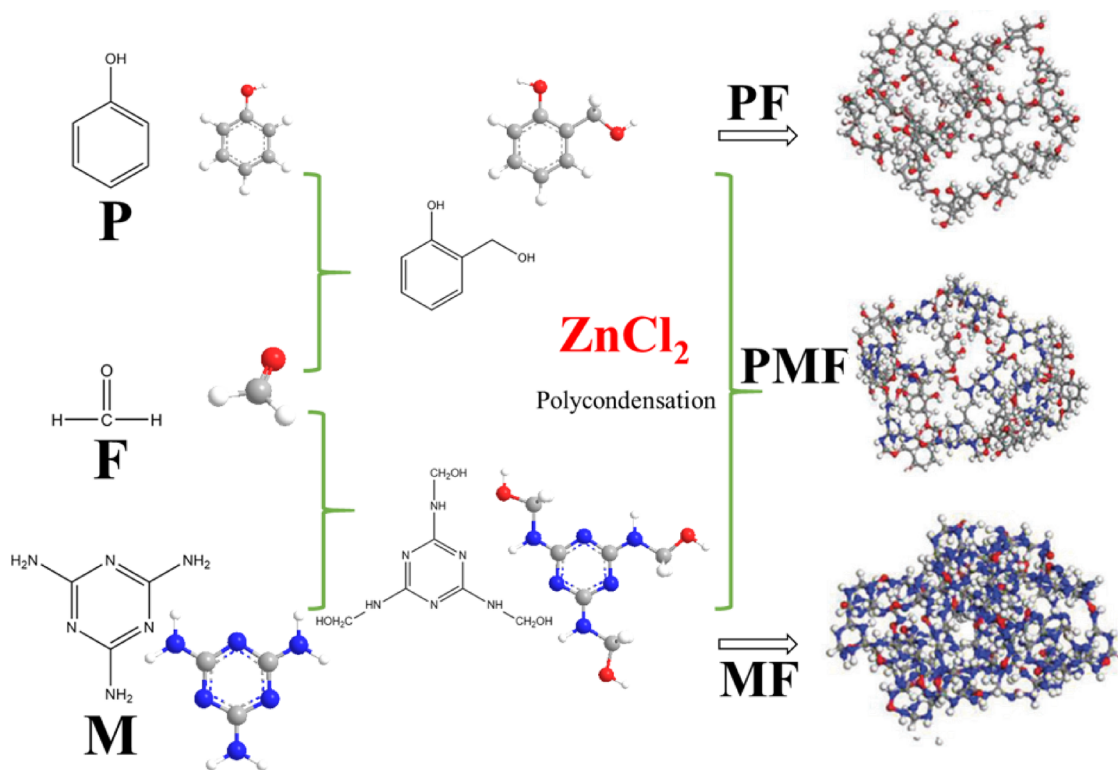
Figure 1. A schematic illustration of the synthetic route of PMF networks.

systems under vigorous stirring followed by the process of formation.

2.4. Characterizations. The morphologies of the PMF and NCA samples were analyzed using a field-emission scanning electron microscope (Nova Nano SEM450, USA). Transmission electron microscopy (TEM) was performed using a Tecnai F 20 instrument operated at 200 kV. The crystalline structure was analyzed via X-ray diffraction (XRD) using a diffractometer with Cu Kα radiation (D/max-2400, Japan), with the source light at a wavelength (λ) of 0.1541 nm. Elemental analyses (EAs) were evaluated with a Vario EL III elemental analyzer (Germany). The surface chemical compositions and functional groups of materials were further investigated via X-ray photoelectron spectroscopy (XPS) (Thermo ESCALAB 250XI, USA) using Al Kα radiation as the X-ray source. The binding energy of elements was calibrated using a C1s photoelectron peak at 284.6 eV. A Raman microscope (Thermo Fisher, USA) and a Fourier transform infrared (FTIR) spectroscope (VERTEX 70-FTIR, Bruker, Germany) were used to survey the surfaces of the PMF and NCA samples. Thermogravimetric (TG) analysis and differential scanning calorimetry were performed using a NETZSCH STA 449 F3 thermobalance at a heating rate of 10 °C min^{-1} from 40 to 900 °C under a nitrogen flow of 20 mL min^{-1}.

Nitrogen adsorption/desorption isotherms were measured at −196 °C with a NOVA-4200e sorption analyzer (Quantachrome). Before measurements, samples (approximately 80 mg) were heated under a vacuum at 200 °C for 2 h. Pore-size distributions were calculated by a quenched solid density functional theory (QSDFT) model. The total pore volume (V_{total}) was calculated from the amount adsorbed at a relative pressure of 0.99. The ultramicropore volume (V_{ultra}, for pore sizes lower than 1 nm) was calculated via the t-plot method.

2.5. CO$_2$ Adsorption Measurements. The static CO$_2$ and N$_2$ adsorption isotherms were measured with a NOVA-4200e sorption analyzer at vacuum pressure, 0 °C, and 25 °C. Before the measurement, 80 mg of the sample was degassed under a vacuum at 200 °C for 2 h. After cooling down to room temperature, the CO$_2$ and N$_2$ adsorption capacity of the sample was analyzed using NOVA-4200e, and the adsorption isotherms of CO$_2$ and N$_2$ were assessed using the molar ratio of the adsorption capacities of CO$_2$ and N$_2$ ranging from 0 to 1.0 bar. The isosteric heat value was estimated from the CO$_2$ adsorption isotherms using the Clausius−Clapeyron equation (eq se1).[43] The selectivity for CO$_2$ from mixtures (CO$_2$/N$_2$ = 15/85 v/v) was calculated by the IAST method (eq se2).[4]

2.6. Dynamic Adsorption and Gas-Mixture Separation Measurements. CO$_2$ and N$_2$ uptakes in dynamic gas-mixture flow by NCA-X were investigated. The breakthrough experiments of gas-mixture CO$_2$/N$_2$ (15:85) of the sorbents were performed on a fixed-bed adsorber (quartz glass tube, with an inner diameter of 4 mm and length of 300 mm) at 25 °C and 1.01 bar. The temperature of the adsorber was controlled by a thermostatic water bath. The adsorbent mass was 0.08 g, and all the samples were pretreated at 200 °C for 12 h before dynamic adsorption experiments. Before the breakthrough experiments, the adsorbent sample was heated at 200 °C for 2 h under argon at a flow rate of 80 mL min^{-1}. The experiment was performed by changing the gas flow from argon to gas-mixture CO$_2$/N$_2$ (15:85) at a flow rate of 2 mL min^{-1} when the sample cooled down to room temperature. The effluent gas was monitored by an Agilent 7890A gas chromatograph (GC) using a thermal conductivity detector (TCD). The blank experiment was conducted in the same condition; the only change is to replace the adsorbent in the fixed bed with quartz sand.

3. RESULTS AND DISCUSSIONS

3.1. Characterization of Organic Aerogels. As shown in Figure 1 and Figure S2, a condensation reaction by the groups of methylol between PF and MF forms methylene and methylene ether bridged polymers. These polymers can be copolymerized to form small clusters that can act as nucleation sites composed of branched polymers. Under hydrothermal conditions, they continuously react with many other unreacted particles to grow into microsphere-type co-condensed particles. This process is thought to be similar to Stöber by monomer addition, in which nucleation is pretty rapid, followed by particle growth without further nucleation.[43] As polymerization goes on, the density and molecular weight of polymers increase as the M/P ratio increases. Steric retardation, chain elongation, and particularly chain branching dramatically reduce polymers' compatibility with water and consequently increase nucleation rates and decrease the time of growth stage.[37] Therefore, smaller microparticulates are formed at a higher M/P ratio. In Figure S3, the volume of PMF-X OAs decreased with a decrease in the M/P ratio. This phenomenon may be attributed to the faster cross-linking reaction of PFs under the catalysis of $ZnCl_2$, which expands the macroscopic porous structure.

The chemical composition of the PMF OAs was investigated by elemental analysis (EA). In Table S1, the EA data show the changes that occurred in the nitrogen content of PMF-X, which indicated that the aforementioned outcomes are in good agreement with the carbon/nitrogen atomic ratio in the precursors.

The successful incorporation of M into the PF network was further confirmed by the Fourier transform infrared (FTIR) spectra (Figure S4), where all PMF samples averaged similar curves. However, a broad band that consisted of $-OH$ and/or $-NH$ molecules at approximately 3400 cm^{-1} and bands at 1547, 1480, and 1340 cm^{-1} attributed to the $C-N$ stretching vibrations in the triazine ring and the carbon−nitrogen breathing mode have been calibrated and identified. All these results proved that the nitrogen atom was smoothly incorporated into the skeleton of PF.

The TG curve of MF shows a low residual weight (5%, Figure 2). This result suggests its poor thermal stability. MF resins have a relatively low thermostability with about 24% weight loss from room temperature to 375 °C that further increases to 86% from 375 to 600 °C. After the copolymerization of MF with PF, the residue was significantly increased. While the PF component increased from 33% (PMF-1-2) to 80% (PMF-4-1), the residual weight was as high
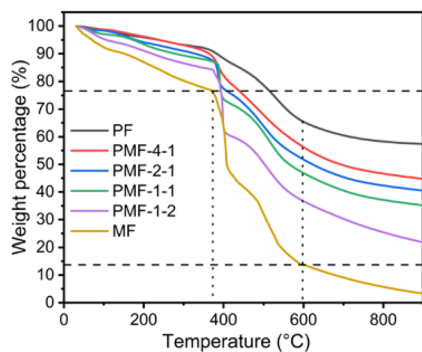
as 20 to 47% of the entire sample at 900 °C. This result suggested the successful copolymerization of PF with MF and the inhibition of the pyrolysis of the latter in the PMF precursor.

3.2. Characterizations of NCAs. NCA-X was synthesized by using PMF-X-Z as the precursor. During the carbonization and activation processes, the PMF-X-Z monolith expanded because $ZnCl_2$ served as a dehydration and foaming agent. Herein, $ZnCl_2$ absorbed moisture from the PMF polymerization process and promoted the formation of PMF networks as a catalyst. Specifically, a large number of micropores were formed by $ZnCl_2$ on the CA obtained from the subsequent carbonization and activation processes. After the removal of ZnO (transformed from $ZnCl_2$) in the activated carbon sample by washing with dilute HCl and direct drying in the air under ambient conditions, a stable, lightweight black NCA-X was obtained.

The mass of $ZnCl_2$ strongly influences the morphology of the PMF-X-Z monolith, and only in a suitable mass range can a homogeneous PMF-X-Z monolith be obtained. Excessive amounts of $ZnCl_2$ will induce a mixed phase, not liquid, and when the $ZnCl_2$ content is too low, the mixed phase could be subsequently separated. The scanning electron microscopy (SEM) images of NCA with different ratios of $ZnCl_2$ are shown in Figure S5. NCA_0-2-1 without $ZnCl_2$ in the pre-polymerization and carbonization−activation steps with a poor microporous network and an extremely low specific area (70− 90 m^2/g). Compared with NCA_0-2-1, the NCA_4-2-1 aerogel exhibits a more defined porosity (type I isotherm) and higher surface area. The NCA_8-2-1 aerogel under hypersaline conditions exhibits the highest surface area, micropore volume, and interconnected porous structure (Table S2). The nanostructure of NCA_8-2-1 was accordingly characterized via SEM. The results showed that the carbon material was composed of fine interconnected carbon frazzles of approximately 10 nm (Figure S5c). By contrast, NCA_0-2-1 without any $ZnCl_2$ resulted only in dense structures. This finding emphasizes the role of $ZnCl_2$ as a surface stabilizer and dispersant.

By referring to the outcomes of SEM and TEM characterizations, we determined that different M/P ratios exert a considerable impact on the microstructure of NCA-X (Figure 3). With an increasing amount of M/P ratio, the small particles that comprise the PMF network exhibited a decrease in diameter. Carbons aerogels have a strongly developed internal surface, and they are usually characterized by a polydisperse capillary structure comprising pores of different sizes and shapes. As illustrated in Figure 4, NCA-2-1 possesses a randomly distributed worm-shaped slit pore structure.

Figure 5a and Figure S6a show the N_2 adsorption−desorption isotherms, and the pore characteristics of the samples were quantified. The pore characteristics of the samples were quantified by measuring N_2 adsorption−− desorption isotherms and CO_2 adsorption isotherms. The structural development of aerogels depends on the composition and synthesis conditions of the precursors, which are critical to their gas adsorption capacity.[44] The nitrogen adsorption isotherm of NCA_0-2-1 is like a type I adsorption isotherm, and the specific surface area (Table S2) is as low as 17 m^2/g, indicating that the material without $ZnCl_2$ was nearly nonporous. The specific surface area of the NCA_4-2-1 and NCA_8-2-1 samples (933 and 1156 m^2/g) is much higher than that of NCA_0-2-1. The increased amount of $ZnCl_2$ in the

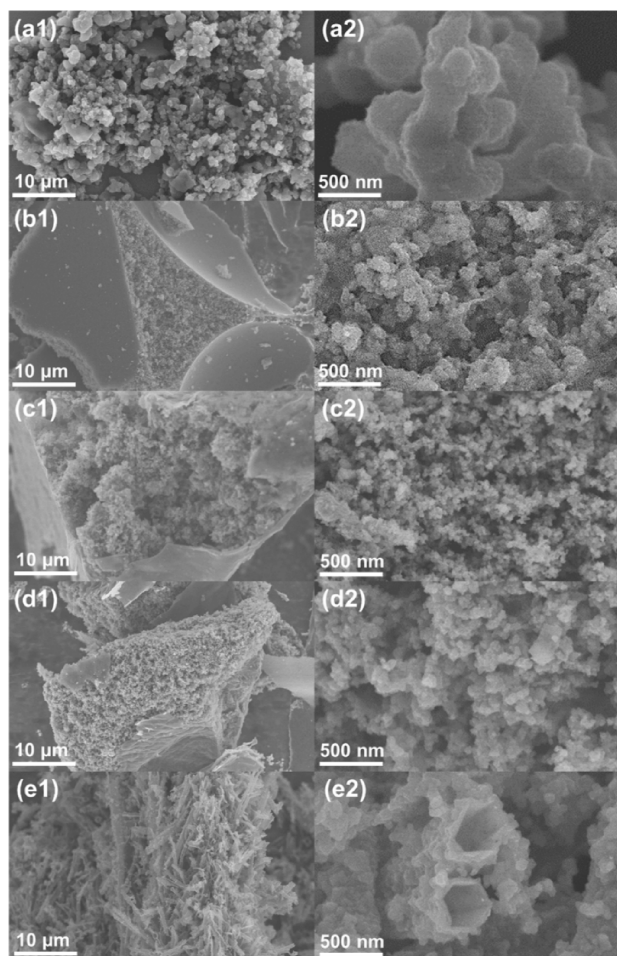**Figure 2.** TG curves of PF, MF, and PMF resins.

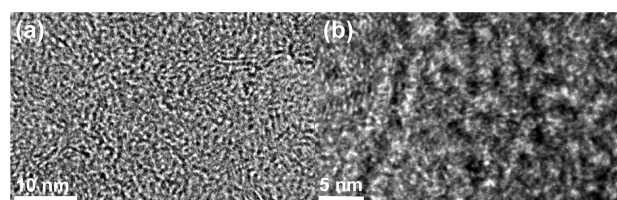**Figure 3.** SEM images of (a) CA, (b) NCA-4-1, (c) NCA-2-1, (d) NCA-1-1, and (e) NCA-1-2.

Figure 4. TEM micrographs of the NCA-2-1.

precursor leads to a hierarchically porous structure of micro- and mesopores during the thermal decomposition process, thereby exhibiting high specific surface area and total pore volume (Figure 5b and Table 1).

In contrast with NCA_0-2-1, the NCA-X samples prepared with a high $ZnCl_2$ content exhibited typical type IV characteristics with a broad capillary condensation step in the relative pressure (P/P_0) range of 0.30−0.70, revealing high mesoporosity. This capillary condensation step shows that the samples exhibit disordered mesopores,[45] which are confirmed further by the PSD (Figure 5b) and the data obtained from the TEM analysis. These data represent that a moderate $ZnCl_2$ content could promote the specific surface area and facilitate the construction of the porous structure and total pore volume. The N-free carbon aerogel CA exhibits a higher specific surface area, and the average pore diameter than NCA-X reveals the presence of smaller mesopores (2−4 nm). For NCA-2-1, the prepolymerized OA shows a more clearly defined porosity (high surface area), suggesting a proper cross-linking of the precursors. For a higher M/P ratio (samples NCA-1-1 and NCA-1-2), the formation of the microporosity is more pronounced (Figure 5b and Table 1). Some authors interpreted similar results in terms of shorter C−N bond lengths that would induce a buckling of the basal plane and consequently a smaller porosity.[44] The increase in the number of micropores is conducive to the adsorption and separation of small molecules of CO_2.[1]

The FTIR spectra of the prepared carbons are shown in Figure 6. A broad band at 3400 cm^{-1} attributed to either −OH and −NH moieties was detected, along with the bands at 1246 and 1600 cm^{-1}. All NCA-X samples showed a small peak at 1246 cm^{-1}, which can be assigned to the stretching vibrations of aromatic C−N bonds. The in-plane N−H deformation vibration at 1600 cm^{-1} was strengthened, which can be interpreted as the nitrogen-rich carbon framework and the activation of the ammonia released from the rupture of triazine rings.[44]

In Figure 7a, a broad peak at 2θ is equal to the XRD pattern of 44° NCA-X, which corresponds to (100) diffracted amorphous carbon. Another extremely weak broad peak intensity was found at approximately $2\theta = 22°$, which can be indexed (002) by diffracted amorphous carbon. The XRD characterization results show that NCA-X exhibits amorphous characteristics and does not have long-term structural order, which is in good agreement with the TEM observations.
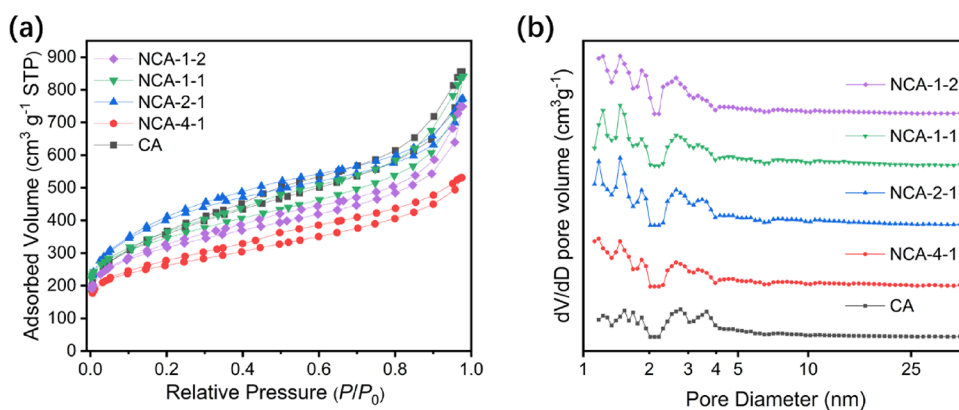

Figure 5. (a) Nitrogen adsorption and desorption curve at −196 °C for the carbon aerogels. (b) Pore size distribution (PSD) curve.

Table 1. Summary of Structural Properties and Chemical Composition of the Carbon Aerogels

sample	S_{BET}[a] $[m^2\ g^{-1}]$	S_{mic} $[m^2\ g^{-1}]$	V_t[b] $[cm^3\ g^{-1}]$	V_{ultra}[c] $[cm^3\ g^{-1}]$	D_p [nm]	N (%) XPS[d]	EA[e]
CA	1295	655	1.13	0.14	2.105	0	0
NCA-4-1	1060	623	1.01	0.14	2.195	3.85	16.8
NCA-2-1	1240	636	1.20	0.18	2.14	3.99	21.8
NCA-1-1	1101	852	1.15	0.20	1.815	5.12	29.7
NCA-1-2	1055	903	1.06	0.22	1.745	6.07	36.5

[a]S_{BET}: specific surface area calculated by the BET method. [b]V_t: total pore volume at P/P_0 = 0.99. [c]V_{ultra}: Ultramicropore volume (<1 nm) was obtained from the CO_2 adsorption branch at 273 K. [d]By XPS results: N at. %. [e]N wt % measured by elemental analysis results of precursors (PMF-X).
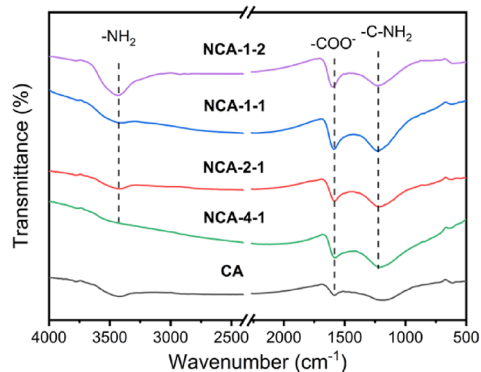
Figure 6. FTIR spectra of NCA samples.
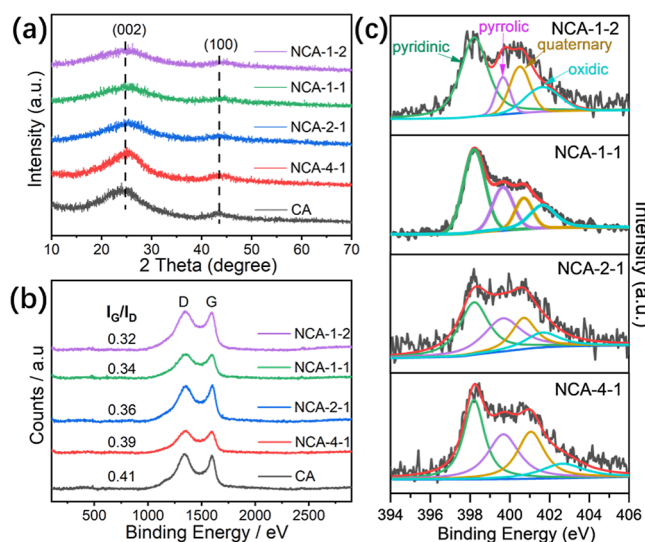
Figure 7. (a) XRD patterns of as-prepared materials after acid treatment. (b) Raman spectra of the obtained materials. (c) High-resolution XPS spectra of the deconvoluted N1s peak.

The structure of NCAs was characterized by Raman spectroscopy (Figure 7b). All samples show the broad bands of the carbon material (D and G bands) between 1000 and 2000 cm^{-1}. The variation of the I_G/I_D ratio can be used to measure ordered changes in the carbon network structure that cannot be detected by classical powder XRD.[45] The integral area values of the D and G peaks are summarized in Table S3 in the Supporting Information. CA without nitrogen exhibited an I_G/I_D value of 0.41, and a meaningful decrease of this ratio from 0.39 to 0.32 was detected when the M/P ratio increased from 1/4 to 2. This finding suggests that an increase in the

ratio of conversion to MF and the incorporation of nitrogen induce the formation of more irregular structures.

The surface chemical states of NCA-X were probed through XPS analysis and are summarized in Figure 7c and Table S4. From the XPS results, the atomic percentages of nitrogen increased from 3.85 at. % in NCA-4-1 to 6.07 at. % in NCA-1-2. Nitrogen 1s spectra can be decomposed into four individual peaks: pyridinic nitrogen (398.2 eV), pyrrolic nitrogen (400.0 eV), quaternary nitrogen (401.2 eV), and oxidic nitrogen (402.5 eV). As the M/P ratio of NCA-X increases, a further increase in nitrogen content (Table S4) follows the expected decrease in the graphitic nitrogen composition and the consequent loss of structural order. Such results agree with the Raman spectroscopy data.

3.3. CO_2 Adsorption. Figure 8a,b shows the CO_2 adsorption isotherms of the five NCA-X samples at 0 and 25 °C. With the M/P ratio increase (from 1/4 to 2/1), the CO_2 adsorption capacities of the NCA-X sorbents are greatly improved, with similar trends at both temperatures. In the range of 0−1 bar, all samples show CO_2 uptake capacity, and no saturation was found. In 1 bar, the NCA-1-2 showed a better CO_2 uptake capacity of 4.30 mmol g^{-1} at 0 °C and 2.65 mmol g^{-1} at 25 °C (Table S5). The amount of CO_2 uptake by NCA-1-2 (4.3 mmol g^{-1}) is nearly double the amount of CO_2 adsorption by CA (2.39 mmol g^{-1}) under the same conditions. This indicates that our modification of the material significantly improved its adsorption capacity for CO_2.

For clarifying the relationship between CO_2 uptake capacity and samples' textural parameters, Figure 8c shows the relationship of CO_2 uptake capacity at 1 bar with the BET surface area and micropore surface area of NCA-X samples. As shown in the figure, the CO_2 uptake capacity is enhanced with the increase of micropore surface areas and V_{ultra}, and it is inversely proportional to D_p overall. In general, the specific surface area and total pore volume of an adsorbent are two of the most important parameters deciding its CO_2 adsorption capability.[46−48] However, in our work, we find that there is no direct linear relationship between the specific surface area/total pore volume of synthesized porous carbons and their CO_2 adsorption amounts. CA has the largest specific surface area, but the CO_2 adsorption capacity is lower than NCA-X. These results suggest that the specific surface area of the material is not the only factor affecting the adsorption capacity of CO_2. Compared with CA (without N content), NCA-1-2 has a lower specific surface area and smaller pore volume but has a higher CO_2 uptake capacity. Notably, the CO_2 capture capacity increased with the increase of the micropore surface area (S_{mic}) (Figure 8a, red line) and ultramicroporous volume ratio (V_{ultra}) (Figure 8d, black line), while it was inversely proportional to S_{BET} and D_p in general. These results suggest a strong positive
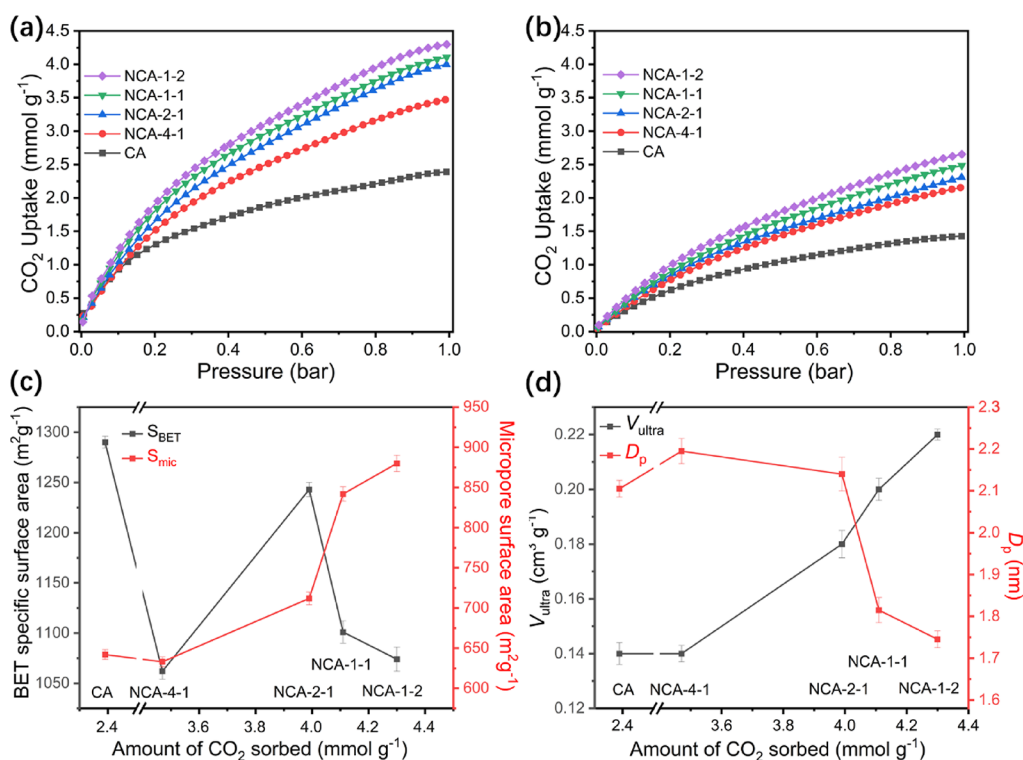
Figure 8. CO_2 adsorption isotherms at (a) 0 °C and (b) 25 °C. Correlation between CO_2 adsorption capacity and textural characteristics of various adsorbents at 0 °C and 1 bar: (c) CO_2 adsorption capacity vs surface areas. (d) CO_2 adsorption capacity vs V_{ultra} (<1 nm) and D_p.
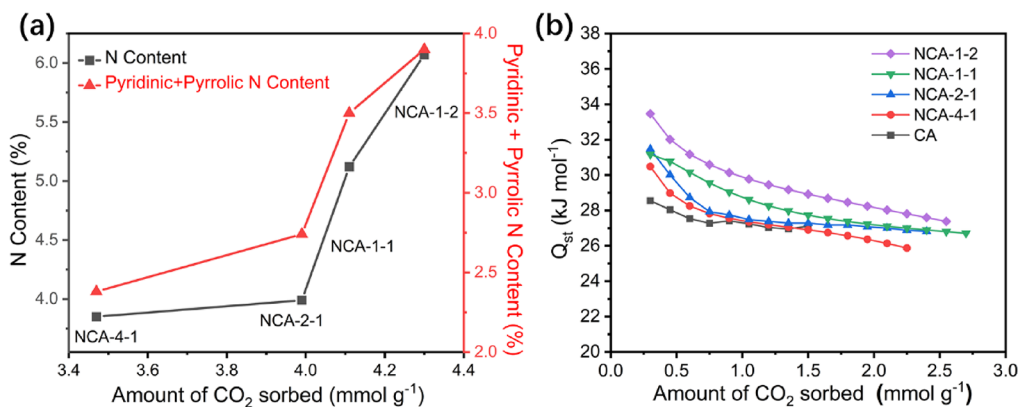

Figure 9. (a) CO_2 adsorption capacity vs N content. (b) Isosteric heat of adsorption at different CO_2 loadings of NCAs.

correlation between the CO_2 capture capacity and the S_{mic} and V_{ultra} of the synthetic porous carbon adsorbents. We assume that a certain number of mesoporous channels provide an ideal environment for the diffusion of CO_2 molecules, and then the ultramicropores around the mesoporous walls generate van der Waals forces for the interaction of carbon structures with CO_2 molecules, which enhances the adsorption of CO_2.[49]

When comparing CA and NCA-4-1 in Figure 8c,d, CA shows a larger specific surface area and micropore specific surface area, a smaller average pore size, and an approximate ultramicroporous volume. However, the adsorption of CO_2 by CA is less than that of NCA-4-1. This is due to the introduction of N doping in NCAs. For carbon-based porous adsorbent materials, nitrogen doping can provide more abundant CO_2 adsorption sites, especially pyridine nitrogen and pyrrole nitrogen. The increase of adsorption sites can effectively improve the adsorption performance of the material

for CO_2 (Figure 9a). This phenomenon can also be confirmed by the data on the isosteric heat of adsorption of the material CO_2.

The isosteric heats of adsorption (Q_{st}) of NCA-X were calculated using the Clausius−Clapeyron equation based on the CO_2 adsorption isotherms at 0 and 25 °C, and the results are shown in Figure 9b. Q_{st} for NCA-X samples varies in the range of 23.5−33.6 kJ mol^{-1}, which is normally ascribed to physisorption. The rapid decrease to a plateau of the initial adsorption heat is driven by the more active nitrogen surface position.[50] CO_2 molecules are preferentially adsorbed on the stronger binding sites. As the number of adsorption increases, only the weaker binding sites remain available. The nitrogen contains groups that act as Lewis bases in the carbon framework, facilitating the interaction with acidic CO_2 molecules. The increase of active sites not only theoretically improves the adsorption efficiency of the material for CO_2 in
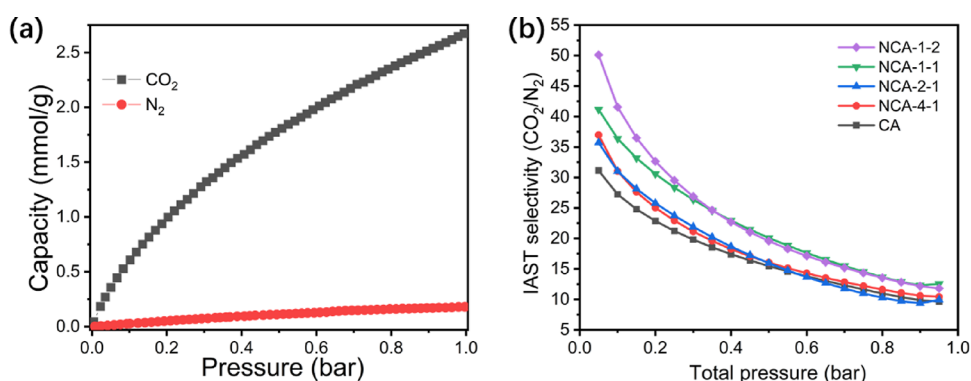
Figure 10. (a) CO_2 and N_2 adsorption isotherms of NCA-1-2 at 25 °C. (b) IAST-predicted adsorption selectivity of CO_2/N_2 at 25 °C.
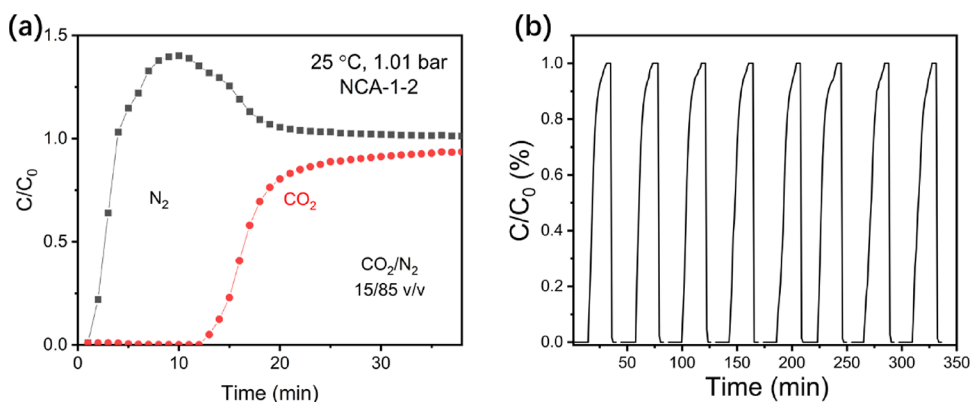

Figure 11. (a) Breakthrough curves of CO_2 sorption at 0 °C using a stream of 15 vol % CO_2 in N_2. (b) Recycle runs of CO_2 adsorption at 25 °C and 1.01 bar, and regeneration.

the low-pressure section but may also be useful for CO_2 selectivity.

3.4. CO_2 Adsorption Selectivity. The CO_2/N_2 adsorption selectivity is an important factor to judge the adsorption separation performance of the material in simulated flue gases. In particular, the adsorption capacity of CO_2 at approximately 0.15 bar and 25 °C can accurately reflect its application in real flue gases.[49] Figure 10a shows the adsorption isotherms of CO_2 and N_2 at 25 °C of sample NCA-1-2. It can be seen that the adsorption capacity of the material for CO_2 is much higher than its capacity for N_2. At 0.15 bar, the CO_2 adsorption of NCA-1-2 (0.81 mmol/g) was about 20 times higher than that of N_2 (0.04 mmol/g). To better visualize the adsorption selectivity of all samples, the CO_2/N_2 selectivity was calculated according to the ideal adsorption solution theory (IAST). The results are shown in Figure 10b. Among all NCA-X samples, NCA-1-2 with an IAST CO_2/N_2 selectivity of 36.5 is the material with the highest selectivity. Such excellent selectivity is mainly due to a large amount of pyridine nitrogen and pyrrole nitrogen (serving as Lewis basic sites) contained in NCA-2-1 (Table S4), which have an essential influence on CO_2/N_2 selectivity.[51,52] The adsorption separation performance of the material was compared with other carbon materials at 25 °C and 0.15 bar, and the selectivity was 36.5, which was similar to or even higher than those recently reported for many carbon-based adsorbents (Table S6).

Adsorption breakthrough experiments were carried out with CO_2/N_2 = 15/85 at 1.01 bar and 25 °C, and the results showed that NCA-1-2 exhibited excellent CO_2 separation performance and verified the conclusions of IAST. As shown in

Figure 11a, N_2 (capacity: 0.16 mmol g^{-1}, 0.85 bar) was released from the adsorption column faster than CO_2 (capacity: 0.77 mmol g^{-1}, 0.15 bar), with a shorter break-through time. The sharp breakthrough curve shows a fast CO_2 adsorption kinetic process, and the adsorption capacity was almost equal to the equilibrium capacity of single component adsorption at 0.15 bar and 25 °C. The N_2 breakthrough curve in Figure 11a showed an obvious "roll-up" during 4 to 17 min, which was due to CO_2 replacing the originally adsorbed N_2 by the adsorbent, and the N_2 concentration in the column was higher than the initial concentration. The results show that NCA-1-2 has excellent CO_2 capture and separation perform-ance and can effectively remove CO_2 from simulated flue gas. The regeneration ability and stability of NCA-1-2 were investigated by eight consecutive adsorption−desorption cycles. As shown in Figure 11b, the almost the same cycle curve shows the excellent CO_2 adsorption performance of NCA-1-2, which can be used as a potential choice for practical industrial application needs.

As shown in Figure S7, the carbon aerogel material is considered to have good hydrophobic properties. We investigated the addition of 3% water vapor to the CO_2/N_2 gas mixture to further observe the dynamic adsorption separation stability of NCA-1-2. The breakthrough experi-ments were carried out with $CO_2/H_2O/N_2$ = 15/3/82 at 1.01 bar and 25 °C. The water vapor in the mixed gas was added by adding a gas circuit with a water saturator at the N_2 inlet to create the mixed gas with the required humidity. Before and after each experiment, the adsorbent was degassed and regenerated using pure helium (He). The sorbent tubes were
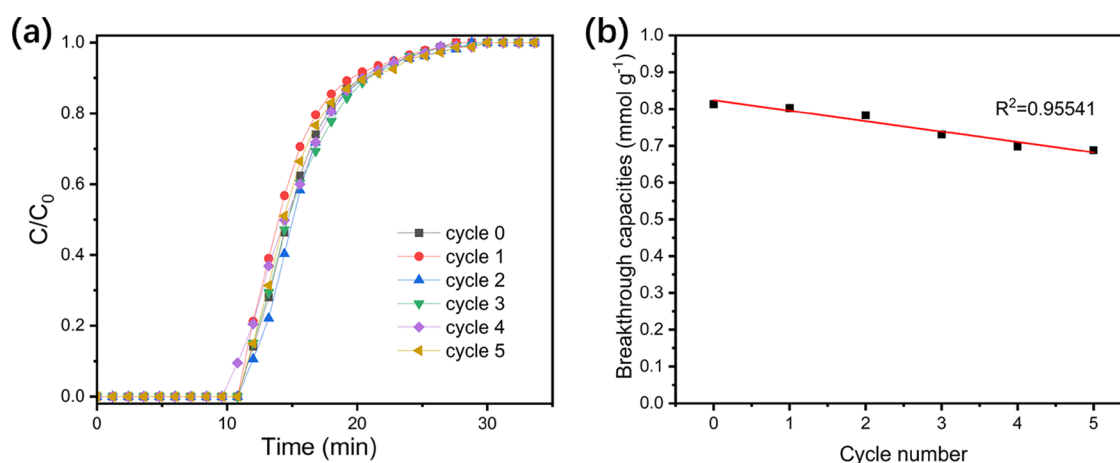
Figure 12. (a) Breakthrough curves of CO_2 adsorption at 25 °C and 1.01 bar using a stream of $CO_2/H_2O/N_2$ = 15/3/82 vol %. Cycle 0 represents dry feed gas. Cycles 1−5 represent wet feed gas. (b) Breakthrough capacities of cyclic experiments with wet feed gas.

heated by a water bath to maintain a constant temperature of 25 °C. The breakthrough curves are illustrated in Figure 12a. Cycle 0 is shown in the figure, representing the experiment with dry gas. After five cycles, the adsorption capacity of CO_2 slowly decreased from 0.81 to 0.69 mmol g^{-1}, still maintaining more than 85% of the adsorption capacity (Figure 12b). This indicates that the hydrophobic nitrogen-doped carbon aerogel material can still maintain a certain efficiency under the influence of 3% water vapor concentration.

4. CONCLUSIONS

In this work, phenol−melamine−formaldehyde resin organic aerogels (PMF) with small gel particles and high N content were obtained by controlling the addition amount of $ZnCl_2$ and the precursor M/P ratio. The homogeneously dispersed $ZnCl_2$ in the organic aerogels can be used as a foaming agent and etching agent directly together with PMF to prepare NCA through the carbonization activation process. Among the prepared samples, NCA-1-2 with a higher micropore specific surface area (903 m^2g^{-1}) and interconnected porous structures contains a large number of pyridinic nitrogen (3.31 at. %) and pyrrolic nitrogen(0.62 at. %). Under the combined effect of surface structure and adsorption sites, NCA-1-2 exhibits the maximum CO_2 adsorption capacity (4.30 mmol g^{-1} at 0 °C) and higher CO_2 adsorption selectivity (36.5 at 25 °C, IAST) toward selective separations of the CO_2/N_2. Specifically, the breakthrough research outcomes indicated great stability and cyclic regeneration performance by eight times CO_2 adsorption running. Under the influence of a 3% concentration of water vapor, NCA can still maintain more than 85% of CO_2 adsorption efficiency after five cycles.

ASSOCIATED CONTENT

Supporting Information

The Supporting Information is available free of charge at https://pubs.acs.org/doi/10.1021/acsomega.2c05072.

> Illustration of the synthesis of NCA from OA; chemical composition of the PMF OAs measured by elemental analysis; FTIR spectra of PMF resins with different P:M ratios; SEM images of NCA-2-1 with varying amounts of $ZnCl_2$: (a) NCA_0-2-1, (b) NCA_4-2-1, (c) NCA_8-2-1; N_2 adsorption and desorption at −196 °C for the NCA_Z-2-1 samples with varying amounts of activator ($ZnCl_2$); pore

size distribution curve; textural properties of the NCA_Z-2-1 samples with varying amounts of $ZnCl_2$; the peak area of Raman spectra; XPS results about surface atomic percentages of nitrogen species of the samples; CO_2 adsorption capacity (mmol CO_2/g) at different temperatures and pressures; and comparison of CO_2/N_2 selectivity of carbon materials with some reported adsorbents (PDF)

AUTHOR INFORMATION

Corresponding Author

Xinyong Li − *State Key Laboratory of Fine Chemicals and Key Laboratory of Industrial Ecology and Environmental Engineering, School of Environmental Science & Technology, Dalian University of Technology, Dalian 116024, China;* ⓘ orcid.org/0000-0002-3182-9626; Phone: +86-411-8470-6658; Email: xyli@dlut.edu.cn

Authors

Liang Wang − *State Key Laboratory of Fine Chemicals and Key Laboratory of Industrial Ecology and Environmental Engineering, School of Environmental Science & Technology, Dalian University of Technology, Dalian 116024, China*

Shiying Fan − *State Key Laboratory of Fine Chemicals and Key Laboratory of Industrial Ecology and Environmental Engineering, School of Environmental Science & Technology, Dalian University of Technology, Dalian 116024, China;* ⓘ orcid.org/0000-0003-1024-6824

Moses O. Tadé − *Department of Chemical Engineering, Curtin University, Perth, WA 6845, Australia*

Shaomin Liu − *Department of Chemical Engineering, Curtin University, Perth, WA 6845, Australia*

Complete contact information is available at:
https://pubs.acs.org/10.1021/acsomega.2c05072

Notes

The authors declare no competing financial interest.

ACKNOWLEDGMENTS

■ REFERENCES

(1) Sevilla, M.; Valle-Vigon, P.; Fuertes, A. B. N-Doped Polypyrrole-Based Porous Carbons for CO_2 Capture. *Adv. Funct. Mater.* **2011**, *21*, 2781−2787.

(2) He, J.; To, J. W. F.; Psarras, P. C.; Yan, H.; Atkinson, T.; Holmes, R. T.; Nordlund, D.; Bao, Z.; Wilcox, J. Tunable Polyaniline-Based Porous Carbon with Ultrahigh Surface Area for CO_2 Capture at Elevated Pressure. *Adv. Energy Mater.* **2016**, *6*, 1502491.

(3) Wang, L.; Li, J.; Gan, G.; Fan, S.; Chen, X.; Liang, F.; Wei, L.; Zhang, Z.; Hao, Z.; Li, X. Activated Carbon Fibers Prepared by One-Step Activation with $CuCl_2$ for Highly Efficient Gas Adsorption. *Ind. Eng. Chem. Res.* **2020**, *59*, 19793−19802.

(4) Zhang, Q.; Zhang, G.; Yan, H.; Zhang, Y.; Liu, J.; Cheng, H. Time-Saving and Cheap Strategy To Prepare Large Mesoporous Materials for Efficient CO_2 Adsorption. *Ind. Eng. Chem. Res.* **2021**, *60*, 9915−9927.

(5) Ko, K. J.; Jin, S.; Lee, H.; Kim, K. M.; Mofarahi, M.; Lee, C. H. Role of Ultra-micropores in CO_2 Adsorption on Highly Durable Resin-Based Activated Carbon Beads by Potassium Hydroxide Activation. *Ind. Eng. Chem. Res.* **2021**, *60*, 14547−14563.

(6) Mashhadimoslem, H.; Vafaeinia, M.; Safarzadeh, M.; Ghaemi, A.; Fathalian, F.; Maleki, A. Development of Predictive Models for Activated Carbon Synthesis from Different Biomass for CO_2 Adsorption Using Artificial Neural Networks. *Ind. Eng. Chem. Res.* **2021**, *60*, 13950−13966.

(7) Deng, J.; Zou, W.; Mi, J.; Du, Z.; Kong, P.; Zhang, C. Construction of Porous Polymer Beads for CO_2 Capture in a Fluidized Bed with High Stability. *Ind. Eng. Chem. Res.* **2021**, *60*, 7624−7634.

(8) De Witte, N.; Denayer, J. F. M.; Van Assche, T. R. C. Effect of Adsorption Duration and Purge Flowrate on Pressure Swing Adsorption Performance. *Ind. Eng. Chem. Res.* **2021**, *60*, 13684−13691.

(9) Lawson, S.; Al-Naddaf, Q.; Newport, K.; Rownaghi, A.; Rezaei, F. Assessment of CO_2/CH_4 Separation Performance of 3D-Printed Carbon Monoliths in Pressure Swing Adsorption. *Ind. Eng. Chem. Res.* **2021**, *60*, 16445−16456.

(10) Ye, Y.; Vega Martin, L.; Sanchez Montero, M. J.; López-Diaz, D.; Velázquez, M. M.; Merchán, M. D. Optimizing the Properties of Hybrids Based on Graphene Oxide for Carbon Dioxide Capture. *Ind. Eng. Chem. Res.* **2022**, *61*, 1332−1343.

(11) Wu, H.; Gong, Q.; Olson, D. H.; Li, J. Commensurate adsorption of hydrocarbons and alcohols in microporous metal organic frameworks. *Chem. Rev.* **2012**, *112*, 836−868.

(12) Li, L.; Lin, R. B.; Krishna, R.; Li, H.; Xiang, S.; Wu, H.; Li, J.; Zhou, W.; Chen, B. Ethane/ethylene separation in a metal-organic framework with iron-peroxo sites. *Science* **2018**, *362*, 443−446.

(13) Wu, Y.; Wang, J.; Muhammad, Y.; Subhan, S.; Zhang, Y.; Ling, Y.; Li, J.; Zhao, Z.; Zhao, Z. Pyrrolic N-enriched carbon fabricated from dopamine-melamine via fast mechanochemical copolymerization for highly selective separation of CO_2 from CO_2/N_2. *Chem. Eng. J.* **2018**, *349*, 92−100.

(14) Chen, C.; Huang, H.; Yu, Y.; Shi, J.; He, C.; Albilali, R.; Pan, H. Template-free synthesis of hierarchical porous carbon with controlled morphology for CO_2 efficient capture. *Chem. Eng. J.* **2018**, *353*, 584−594.

(15) Li, H.; Li, J.; Thomas, A.; Liao, Y. Ultra-High Surface Area Nitrogen-Doped Carbon Aerogels Derived From a Schiff-Base Porous Organic Polymer Aerogel for CO_2 Storage and Supercapacitors. *Adv. Funct. Mater.* **2019**, *29*.

(16) Wang, H.; Cheng, Z.; Liao, Y.; Li, J.; Weber, J.; Thomas, A.; Faul, C. F. J. Conjugated Microporous Polycarbazole Networks as Precursors for Nitrogen-Enriched Microporous Carbons for CO_2 Storage and Electrochemical Capacitors. *Chem. Mater.* **2017**, *29*, 4885−4893.

(17) Hao, G. P.; Li, W. C.; Qian, D.; Wang, G. H.; Zhang, W. P.; Zhang, T.; Wang, A. Q.; Schuth, F.; Bongard, H. J.; Lu, A. H. Structurally Designed Synthesis of Mechanically Stable Poly-(benzoxazine-co-resol)-Based Porous Carbon Monoliths and Their Application as High-Performance CO_2 Capture Sorbents. *J. Am. Chem. Soc.* **2011**, *133*, 11378−11388.

(18) Yang, X.; Cheng, C.; Wang, Y.; Qiu, L.; Li, D. Liquid-mediated dense integration of graphene materials for compact capacitive energy storage. *Science* **2013**, *341*, 534−537.

(19) Chu, Z.; Feng, Y.; Seeger, S. Oil/water separation with selective superantiwetting/superwetting surface materials. *Angew. Chem. Int. Ed.* **2015**, *54*, 2328−2338.

(20) Xie, P. T.; Sun, W.; Liu, Y.; Du, A.; Zhang, Z. D.; Wu, G. M.; Fan, R. H. Carbon aerogels towards new candidates for double negative metamaterials of low density. *Carbon* **2018**, *129*, 598−606.

(21) Huang, Y. J.; Lin, Y. J.; Chien, H. J.; Lin, Y. F.; Ho, K. C. A Pt-free pristine monolithic carbon aerogel counter electrode for dye-sensitized solar cells: up to 20% under dim light illumination. *Nanoscale* **2019**, *11*, 12507−12516.

(22) Maleki, H.; Husing, N. Current status, opportunities and challenges in catalytic and photocatalytic applications of aerogels: Environmental protection aspects. *Appl. Catal. B* **2018**, *221*, 530−555.

(23) Liu, K. L.; Jiao, M. L.; Chang, P. P.; Wang, C. Y.; Chen, M. M. Pitch-based porous aerogel composed of carbon onion nanospheres for electric double layer capacitors. *Carbon* **2018**, *137*, 304−312.

(24) Li, Y.; Liu, X. F.; Nie, X. Y.; Yang, W. W.; Wang, Y. D.; Yu, R. H.; Shui, J. L. Multifunctional Organic-Inorganic Hybrid Aerogel for Self-Cleaning, Heat-Insulating, and Highly Efficient Microwave Absorbing Material. *Adv. Funct. Mater.* **2019**, *29*, 1807624.

(25) Hou, Y.; Li, J.; Gao, X.; Wen, Z.; Yuan, C.; Chen, J. 3D dual-confined sulfur encapsulated in porous carbon nanosheets and wrapped with graphene aerogels as a cathode for advanced lithium sulfur batteries. *Nanoscale* **2016**, *8*, 8228−8235.

(26) Yan, C.; Meng, N.; Lyu, W.; Li, Y.; Wang, L.; Liao, Y. Hierarchical porous hollow carbon spheres derived from spirofluor-ene- and aniline-linked conjugated microporous polymer for phase change energy storage. *Carbon* **2021**, *176*, 178−187.

(27) Pekala, R. W.; Farmer, J. C.; Alviso, C. T.; Tran, T. D.; Mayer, S. T.; Miller, J. M.; Dunn, B. Carbon aerogels for electrochemical applications. *J. Non-Cryst. Solids* **1998**, *225*, 74−80.

(28) Reuss, M.; Ratke, L. Subcritically dried RF-aerogels catalysed by hydrochloric acid. *J. Sol-Gel Sci. Technol.* **2008**, *47*, 74−80.

(29) Yu, Z. L.; Li, G. C.; Fechler, N.; Yang, N.; Ma, Z. Y.; Wang, X.; Antonietti, M.; Yu, S. H. Polymerization under Hypersaline Conditions: A Robust Route to Phenolic Polymer-Derived Carbon Aerogels. *Angew. Chem., Int. Ed.* **2016**, *55*, 14623−14627.

(30) Zhao, Y.; Zhao, L.; Yao, K.; Yang, Y.; Zhang, Q.; Han, Y. Novel porous carbon materials with ultrahigh nitrogen contents for selective CO_2 capture. *J. Mater. Chem.* **2012**, *22*, 19726−19731.

(31) Xing, W.; Liu, C.; Zhou, Z.; Zhang, L.; Zhou, J.; Zhuo, S.; Yan, Z.; Gao, H.; Wang, G.; Qiao, S. Z. Superior CO_2 uptake of N-doped activated carbon through hydrogen-bonding interaction. *Energy Environ. Sci.* **2012**, *5*, 7323−7327.

(32) Wei, X.; Wan, S.; Gao, S. Self-assembly-template engineering nitrogen-doped carbon aerogels for high-rate supercapacitors. *Nano Energy* **2016**, *28*, 206−215.

(33) Zeng, F. Y.; Sui, Z. Y.; Liu, S.; Liang, H. P.; Zhan, H. H.; Han, B. H. Nitrogen-doped carbon aerogels with high surface area for supercapacitors and gas adsorption. *Mater. Today Commun.* **2018**, *16*, 1−7.

(34) Yue, L.; Rao, L.; Wang, L.; Sun, Y.; Wu, Z.; DaCosta, H.; Hu, X. Enhanced CO_2 Adsorption on Nitrogen-Doped Porous Carbons Derived from Commercial Phenolic Resin. *Energy Fuels* **2018**, *32*, 2081−2088.

(35) Choi, S. W.; Tang, J.; Pol, V. G.; Lee, K. B. Pollen-derived porous carbon by KOH activation: Effect of physicochemical structure on CO_2 adsorption. *J. CO2 Util.* **2019**, *29*, 146−155.

(36) Zhu, G.; Ma, L.; Lv, H.; Hu, Y.; Chen, T.; Chen, R.; Liang, J.; Wang, X.; Wang, Y.; Yan, C.; Tie, Z.; Jin, Z.; Liu, J. Pine needle-derived microporous nitrogen-doped carbon frameworks exhibit high performances in electrocatalytic hydrogen evolution reaction and supercapacitors. *Nanoscale* **2017**, *9*, 1237−1243.

(37) Sethia, G.; Sayari, A. Comprehensive study of ultra-microporous nitrogen-doped activated carbon for CO_2 capture. *Carbon* **2015**, *93*, 68−80.

(38) Guo, L. P.; Hu, Q. T.; Zhang, P.; Li, W. C.; Lu, A. H. Polyacrylonitrile-Derived Sponge-Like Micro/Macroporous Carbon for Selective CO_2 Separation. *Chemistry* **2018**, *24*, 8369−8374.

(39) Zhou, H.; Xu, S.; Su, H.; Wang, M.; Qiao, W.; Ling, L.; Long, D. Facile preparation and ultra-microporous structure of melamine-resorcinol-formaldehyde polymeric microspheres. *Chem. Commun.* **2013**, *49*, 3763−3765.

(40) Yu, Z. L.; Yang, N.; Zhou, L. C.; Ma, Z. Y.; Zhu, Y. B.; Lu, Y. Y.; Qin, B.; Xing, W. Y.; Ma, T.; Li, S. C.; Gao, H. L.; Wu, H. A.; Yu, S. H. Bioinspired polymeric woods. *Sci. Adv.* **2018**, *4*, eaat7223.

(41) Fiset, E.; Rufford, T. E.; Seredych, M.; Bandosz, T. J.; Hulicova-Jurcakova, D. Comparison of melamine resin and melamine network as precursors for carbon electrodes. *Carbon* **2015**, *81*, 239−250.

(42) Chang, B.; Shi, W.; Han, S.; Zhou, Y.; Liu, Y.; Zhang, S.; Yang, B. N-rich porous carbons with a high graphitization degree and multiscale pore network for boosting high-rate supercapacitor with ultrafast charging. *Chem. Eng. J.* **2018**, *350*, 585−598.

(43) Yang, H.; Luo, M.; Chen, X.; Zhao, X.; Lin, J.; Hu, D.; Li, D.; Bu, X.; Feng, P.; Wu, T. Cation-Exchanged Zeolitic Chalcogenides for CO_2 Adsorption. *Inorg. Chem.* **2017**, *56*, 14999−15005.

(44) Liu, L.; Xie, Z. H.; Deng, Q. F.; Hou, X. X.; Yuan, Z. Y. One-pot carbonization enrichment of nitrogen in microporous carbon spheres for efficient CO_2 capture. *J. Mater. Chem. A* **2017**, *5*, 418−425.

(45) Rasines, G.; Lavela, P.; Macias, C.; Zafra, M. C.; Tirado, J. L.; Parra, J. B.; Ania, C. O. N-doped monolithic carbon aerogel electrodes with optimized features for the electrosorption of ions. *Carbon* **2015**, *83*, 262−274.

(46) Jiang, Z.; He, C.; Dummer, N. F.; Shi, J. W.; Tian, M.; Ma, C.; Hao, Z.; Taylor, S. H.; Ma, M. D.; Shen, Z. X. Insight into the efficient oxidation of methyl-ethyl-ketone over hierarchically micro-mesostructured Pt/K-(Al)SiO$_2$ nanorod catalysts: Structure-activity relationships and mechanism. *Appl. Catal., B* **2018**, *226*, 220−233.

(47) Lee, J. W.; Balathanigaimani, M. S.; Kang, H. C.; Shim, W. G.; Kim, C.; Moon, H. Methane storage on phenol-based activated carbons at (293.15, 303.15, and 313.15) K. *J. Chem. Eng. Data* **2007**, *52*, 66−70.

(48) Furukawa, H.; Ko, N.; Go, Y. B.; Aratani, N.; Choi, S. B.; Choi, E.; Yazaydin, A. O.; Snurr, R. Q.; O'Keeffe, M.; Kim, J.; Yaghi, O. M. Ultrahigh Porosity in Metal-Organic Frameworks. *Science* **2010**, *329*, 424−428.

(49) Chen, C.; Yu, Y.; He, C.; Wang, L.; Huang, H.; Albilali, R.; Cheng, J.; Hao, Z. Efficient capture of CO_2 over ordered micro-mesoporous hybrid carbon nanosphere. *Appl. Surf. Sci.* **2018**, *439*, 113−121.

(50) Aijaz, A.; Fujiwara, N.; Xu, Q. From Metal-Organic Framework to Nitrogen-Decorated Nanoporous Carbons: High CO_2 Uptake and Efficient Catalytic Oxygen Reduction. *J. Am. Chem. Soc.* **2014**, *136*, 6790−6793.

(51) Chen, B.; Ma, G.; Kong, D.; Zhu, Y.; Xia, Y. Atomically homogeneous dispersed ZnO/N-doped nanoporous carbon composites with enhanced CO_2 uptake capacities and high efficient organic pollutants removal from water. *Carbon* **2015**, *95*, 113−124.

(52) Li, L.; Wang, Y.; Gu, X.; Yang, Q.; Zhao, X. Increasing the CO_2/N_2 Selectivity with a Higher Surface Density of Pyridinic Lewis Basic Sites in Porous Carbon Derived from a Pyridyl-Ligand-Based Metal-Organic Framework. *Chem.-Asian. J.* **2016**, *11*, 1913−1920.